

Study of Corrosion Behavior of X80 Steel in Clay Soil with Different Water Contents under HVDC Interference

Zhenchang Xu, Yanxia Du*, Runzhi Qin, Hui Zhang

Institute for Advanced Materials and Technology, University of Science and Technology Beijing, Beijing, 10083, China

*E-mail: duyanxia@ustb.edu.cn

Received: 6 April 2019 / Accepted: 20 June 2019 / Published: 10 April 2020

With the large-scale construction of high voltage direct current systems, high voltage direct current (HVDC) interference on long-distance pipelines has become increasingly serious. The field tests showed that the pipe-to-soil potential caused by the HVDC interference could be several hundred volts. Thus, investigating the corrosion behavior of pipelines under such large potential has become an urgent problem in the industry. In this study, the corrosion behavior of X80 steel in clay soil with different water contents at a potential of 100 V produced by the HVDC interference was studied by laboratory simulation experiments. The results showed that the corrosion rates of X80 steel with different soil water contents were quite different. At the soil water contents of 17%, 21%, 25.5%, 30.5%, and 34.5%, the corrosion rates were 1.69, 10.77, 31.67, 85.13, and 169.49 $\mu\text{m}\cdot\text{h}^{-1}$, respectively. At the same time, the direct current density of the samples was found to be quite different under different soil water contents. At the soil water content <30.5%, the current density reached sharply to a peak value in a short time when the high DC interference potential was applied, then it dropped rapidly to a lower steady value and maintained for a long time near the stable value, the steady value was less than one fifth of the peak value. At the soil water content >30.5%, the current density gradually increased to a peak value, and maintained near the high peak value. The changes in the soil temperature, water content, and resistivity near the samples under interference were analyzed, indicating that the rapid decrease in the current density at lower water content was because of increasing soil temperature near the sample surface, the decrease in the soil water content, and the increase in the spread resistance. The morphologies of the corrosion products at different water contents were characterized by X-ray diffraction and scanning electron microscopy. The results showed that when the water content was 17%, the main corrosion product was α -FeOOH. In addition, with increasing water content, various types of FeOOH began to appear, and γ -FeOOH was the main product. When the water content increased to 34.5%, the main product transformed to Fe_2O_3 . The analyses showed that the difference in the corrosion products under different water contents was closely related to the different current density behaviors of X80 steel under HVDC interference in different soils.

Keywords: HVDC interference; soil water content; corrosion rate; corrosion products; current density

1. INTRODUCTION

High voltage direct current (HVDC) transmission has the advantages of low loss, low cost, and high stability for the current transmission of long distance [1–4]; therefore, large-scale HVDC systems have been constructed in China in recent years. In general, there are two main operation modes of HVDC systems: monopolar operation mode and bipolar operation mode. The normal operation of the system is bipolar, and the unbalanced current generated by it is generally less than 1% of the rated current. However, if one of the poles fails or is repaired, it will operate in the monopolar mode and take the earth as the circuit. At this time, several thousand amperes of direct current (DC) will be injected into the earth through the grounding electrode and might cause significant harm to the metal pipe systems nearby.

In recent years, many cases of HVDC interference suffered by buried pipelines have been reported. Caroli [5] tested a Brazilian pipeline interfered by a ± 600 kV Itaipu HVDC system. The results showed that the maximum pipe-to-soil potential of the pipeline shifted to 46 V_{CSE}, exceeding the human safety voltage. Nicholson [6] tested a pipeline interfered by the Quebec-New England Intertie HVDC system. The results showed that the pipe-to-soil potential deviated to 900 mV. Moreover, with increasing construction of HVDC systems in China, HVDC interference has been detected in a lot of buried pipelines. In the Guangdong province, when one grounding electrode of the HVDC system worked in the monopolar mode and discharged 3200 A current, the pipe-to-soil potential of the pipeline at the place approximately 7 km away from the grounding electrode shifted to 304 V_{CSE} [7]. When the grounding electrode discharged 1200 A, the pipe-to-soil potential of the pipeline shifted to approximately 100 V_{CSE}, exceeding the human safety voltage and affecting the safety of the staff working near the pipeline [8]. In Xinjiang province, Bi [9] tested the West-East natural gas transmission pipeline interfered by the Hami electrode, and the polarization potential of the pipeline at about 35 km away from the grounding electrode shifted to about 0.5 V_{CSE}, indicating a high risk of corrosion.

A large number of field cases showed that HVDC interference can cause large deviation in pipe-to-soil potential. However, the effect of this potential deviation on the corrosion process under this interference has not been clearly understood. Therefore, some studies have been carried out by indoor simulation experiments in recent years. For example, Qin [10] studied the corrosion behavior of X80 steel in Guangdong soil under HVDC interference. The results showed that under 50–300 V DC interference voltages, the current density changed with time in three typical stages. First, the current density rose sharply to a peak value in a few seconds, then it gradually decreased to a stable value, and finally stayed at the stable value for a long time. The biggest corrosion rate was found as 10.63 $\mu\text{m}\cdot\text{h}^{-1}$ under 200 V HVDC interference potential. Fu [11] studied the corrosion regularity of Q235 steel in Hainan soil under DC stray current corrosion. The results showed that the corrosion rate of Q235 was 16.71 $\text{mm}\cdot\text{a}^{-1}$ at an average current density of 14.2 $\text{A}\cdot\text{m}^{-2}$, and the corrosion products mainly composed of Fe₃O₄ and Fe₂O₃, with a small amount of FeS. Qian [12] studied the corrosion behavior of pipeline steel in an extracted soil solution under different DC current densities. The result showed that the

corrosion rate was $12.5 \text{ mm}\cdot\text{a}^{-1}$ when the current density was $10 \text{ A}\cdot\text{m}^{-2}$ and was 31 times of that without DC interference.

These studies show that the corrosion caused by HVDC interference in the soil environment is much more serious than other types of DC interference. Considering the complexity of the soil environment, the characteristics of soil greatly affect the corrosion behavior. Soil water content is an important factor affecting the soil characteristics. The existence of water makes soil function as an electrolyte, providing conditions for the formation of corrosion cell. In contrast, water changes the physical and chemical properties of soil and has a great effect on the corrosion behavior [13,14]. Xu [15] suggested that within a certain range, with increasing water content, the soluble salts in soil dissolve more completely, thus increasing the corrosion rate. They also showed that different soil water contents were closely related to corrosion. However, the interference regularity and corrosion behavior of X80 steel in soil with different water contents under HVDC interference are still unclear.

In this study, indoor simulation experiments were designed to study the corrosion behavior of X80 steel under HVDC interference in clay soil with different water contents by testing the corrosion weight loss, corrosion morphology and characterization of products, monitoring interference parameters and testing soil properties.

2. EXPERIMENTAL

2.1. Material preparation

The working electrode material was X80 pipeline steel, with the metallurgical structure as a combination of ferrite and pearlite. The chemical composition is shown in Table 1. The shape of the sample was a cylinder and the dimensions were $\Phi 18.0 \times 3.0 \text{ mm}^2$. Before the experiment, the surface of the sample was polished step by step to 1000 grit with SiC abrasive paper, making the surface smooth without obvious scratches. After that, the samples were cleaned with acetone, ethyl alcohol, and deionized water and then dried. Besides, electronic balance (FA2004B, accuracy is 0.1 mg) was used to weigh and record the samples before the experiment. In the experiment, the samples were sealed by a special type polytetrafluoroethylene fixture, and the exposure area of the metal was 1 cm^2 .

Table 1. Chemical composition in weight percentage (wt%) of X80 pipeline steel

C	Mn	Si	Ni	Cu	Nb	Ti	S	P	Mo	Fe
0.070	1.61	0.21	0.12	0.14	0.041	0.012	0.0025	0.0081	0.13	Balance

The soil used in the experiment was reddish-brown clay soil in Sichuan province and collected 1 m deep underground in the field. The water content was 19%, and the soil resistivity was $27.7 \Omega\cdot\text{m}$. The pH of the soil was 6.5. The ion concentration was measured by dissolving 5 g soil in 30 mL deionized water. The ionic composition is listed in Table 2. Before the experiment, the soil was milled

to fine particles, and the deionized water was added to prepare soil samples with 17%, 21%, 25.5%, 30.5%, 34.5% and 42% water content.

Table 2. Ionic composition of the extracted soil solution, $\text{mg}\cdot\text{L}^{-1}$

SO_4^{2-}	Cl^-	NO_3^-	Na^+	K^+	Ca^{2+}	Mg^{2+}
12.2	1.87	33.4	1.4	0.91	12.1	1.2

2.2. Experimental equipment

The experimental equipment is shown in Figure 1. The dimensions of the test box were $20 \times 10 \times 8 \text{ cm}^3$. The interference circuit included an HSPY 400-01 HVDC interference power source, 10Ω resistance, working electrode (WE), reference electrode (RE), and counter electrode (CE). The WE was an X80 steel fixture; the CE was a piece of red copper with the sizes of $10 \times 8 \times 0.1 \text{ cm}^3$; and the RE was saturated calomel electrode (SCE). All the electrodes were placed in the test box, entirely filled with soil, and a thermometer was immersed at a distance of 1 cm from the WE. The shunt resistor of 10Ω was in series with the interference circuit, and a voltmeter was parallelly connected to the shunt resistor to monitor the voltage, which was used to calculate the DC current in the interference circuit. The frequency of the voltmeter was 1 s. Furthermore, the electrochemical measurement was tested using a Gamry Reference 3000 electrochemical workstation.

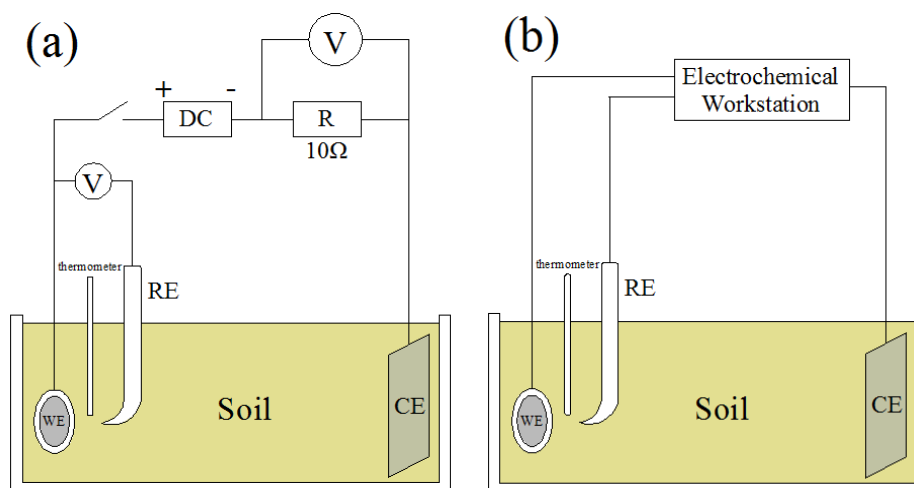


Figure 1. Schematic of experimental equipment (a), and electrochemical measurement system (b)

2.3. Test methods

After the experimental equipment was established, it should stand a while until the open-circuit potential of X80 steel sample gets stabilized. After that, the interference was applied by the power source for 1 h, and the potential between the working electrode and the reference electrode was 100 V.

2.3.1. Local soil environmental properties test of samples

In order to investigate the variation in the local soil environment around samples during HVDC interference, the changes in the soil spread resistance, pH, water content, and the temperature of the local soil before and after the HVDC interference were measured.

The soil spread resistance (R_{spread}) represents the resistance change between the sample and the reference electrode, reflecting the properties of the local environment of the sample and is related to the shape, size, and surface soil resistivity of the sample. When the external current was high or the soil resistivity was high, the potential measured by the reference electrode contained a higher IR drop and could not be neglected. However, R_{spread} could be measured by applying an alternative current (AC) signal by the workstation [16–19], as shown by the following formula:

$$R_{spread} = \frac{U_{AC}}{J_{AC}} \quad (1)$$

where R_{spread} represents the soil spread resistance ($\Omega \cdot cm^2$), U_{AC} is the AC voltage (V), and J_{AC} is the AC density ($A \cdot cm^{-2}$). In the experiment, the R_{spread} was measured using the workstation, and the AC density and the frequency of the AC were $0.0001 A \cdot cm^{-2}$ and 50 Hz, respectively.

During the interference, the soil temperature was measured using a thermometer. After the interference, a small patch of soil near the surface of the sample was taken out and weighed. Then, a small amount of deionized water was dripped on the soil surface contacted with the sample and pH test paper was dipped to obtain the change in the pH value of the local environment of the sample. Finally, the small soil sample was dried and weighed to measure the change in the soil water content.

2.3.2. Corrosion rate test

After the interference, the rust layer on the sample surface was cleaned with the aqueous hydrochloric acid solution, prepared by dissolving 500 mL concentrated hydrochloric acid and 5 g hexamethylenetetramine in 500 mL deionized water. After that, the samples were washed with deionized water and anhydrous ethanol and then dried. The corrosion weight loss was measured using an electronic balance with an accuracy of 0.1 mg, and the corrosion rate was calculated by the following formula:

$$V_{corr} = 10000 * \frac{W_0 - W}{St\rho} \quad (2)$$

where V_{corr} represents the corrosion rate ($\mu m \cdot h^{-1}$), W_0 is the weight before the interference (g), and W is the weight after cleaning (g), S is the exposed area of the sample (cm^2), t is the interference time (h), and ρ is the density of X80 steel ($g \cdot cm^{-3}$).

2.3.3 Corrosion products test

After the interference, the sample was taken out, and the floating soil on the sample surface was cleaned using a brush. Then the macroscopic corrosion morphology was observed by a camera. The physical property was characterized by X-ray diffraction (XRD), conducted using an X-ray diffractometer (D8Advance Bruker, Germany) equipped with Cu Ka radiation. The scan rate was 6

$^{\circ}/\text{min}$, and the 2θ angle was $10\text{-}90^{\circ}$. The surface morphology was characterized by scanning electron microscopy (SEM, GSM-6510A).

3. RESULTS

3.1. Variation in the DC density under HVDC interference

The DC densities of X80 steel in clay soil with different water contents under 100 V HVDC interference are shown in Figure 2(a), indicating that the DC density of the samples had the same trend at the soil water content less than 30.5%. The variation in the current density with time could be divided into three stages [10,11], and it reached sharply to a peak value in a short time at first, then it dropped rapidly to a lower steady value and maintained for a long time near the stable value, and the steady value was less than one fifth of the peak value. Taking the case of 21% soil water content, the variation in the current density is shown in Figure 2(b). The changes in the three stages are as follows: when the high DC interference potential was applied, the DC current density of the sample reached sharply to a peak value in about 8 s, and the peak value was about $678 \text{ A}\cdot\text{m}^{-2}$ at stage 1. Then the DC current density dropped rapidly to a lower steady value in about 600 s and the downward trend was an exponential type, which was the stage 2. Lastly, the DC current density maintained for a long time near the stable value for the rest of time, and the steady value was about $80 \text{ A}\cdot\text{m}^{-2}$ at stage 3. The calculation showed that the steady value was only 11.8% of the peak value. Besides, the peak value and the steady value of the current density were positively correlated with the soil water content. The current density increased with increasing water content.

When the soil water content was $>30.5\%$, the variation in the current density with time could be divided into two stages: (i) it reached sharply to a peak value in a short time, and (ii) it maintained at a high level all the time. The variation in the current density of the three stages disappeared.

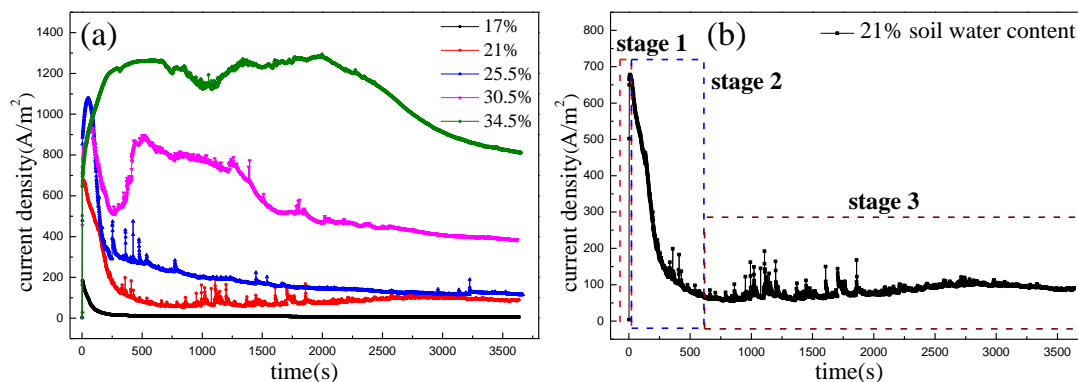


Figure 2. Variation in DC density of X80 steel in clay soil with different water contents under 100 V interference (a), and the variation in the three stages of 21% soil water content (b)

3.2. Variation of local soil environmental properties after HVDC interference

The variation in the R_{spread} measured before and after the interference is shown in Figure 3. Before the interference, the R_{spread} decreased gradually with increasing water content and ranged from $3616 \Omega \cdot cm^2$ to a few hundred. After the interference, the R_{spread} was larger than that before the interference, and the growth of R_{spread} decreased with increasing water content. For example, at 17% water content, the R_{spread} after the interference was 6.9 times of that before the interference; when the water content of the soil was 25.5%, the R_{spread} after the interference was 2.4 times of that before the interference; and the R_{spread} after the interference was only 1.1 times of that before the interference at a water content of 34.5%.

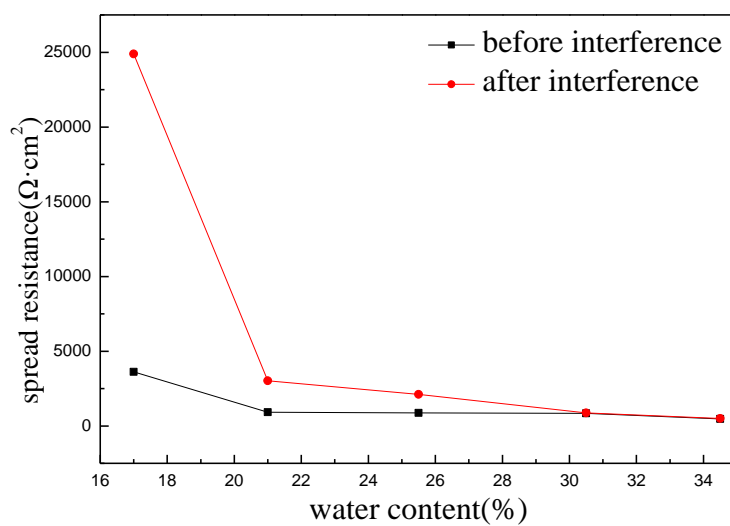


Figure 3. Variation in soil spread resistance before and after the interference

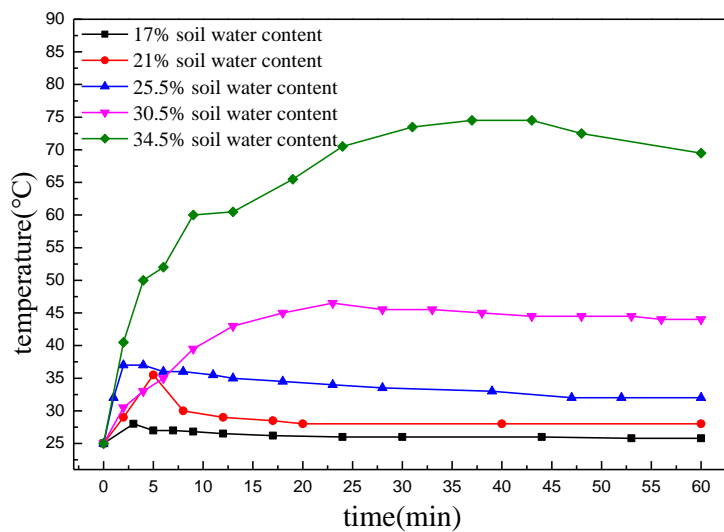


Figure 4. Variation in the local soil temperature near of the sample in clay soil with different water contents under 100 V interference

The change in temperature was recorded during the interference. Figure 4 shows that at the soil water content $<30.5\%$, the temperature increased first and then decreased. If the soil water content was $>30.5\%$, the temperature always remained at a higher level. The highest temperature reached in the interference process of soil sample with 34.5% water content, and the temperature was about $74.5\text{ }^{\circ}\text{C}$. Notably, the thermometer was immersed at a distance of 1 cm from the sample in order to reduce the effect on current distribution. Therefore, the measured temperature was lower than the actual temperature of the sample surface.

After the interference, a small patch of soil near the surface of the sample was taken out and dried, and its water content was measured (w_1). Then, w_1 was compared to the original soil water content (w_0). Figure 5(a) shows that the soil water content near the surface of the sample decreased first, and then increased slightly. When the original soil water content was 25.5% , the soil water content after 1 h interference was the lowest and was about 12% . The reduction in the water content ($w_0 - w_1$) was obtained by subtracting the soil water content after the interference from the original soil water content. The results shown in Figure 5(b) indicate that the reduction in the water content increased gradually with the original soil water content. At 17% original soil water content, the reduction in the water content was only about 3.4% . At 34.5% original soil water content, the reduction in the water content was about 20.7% .

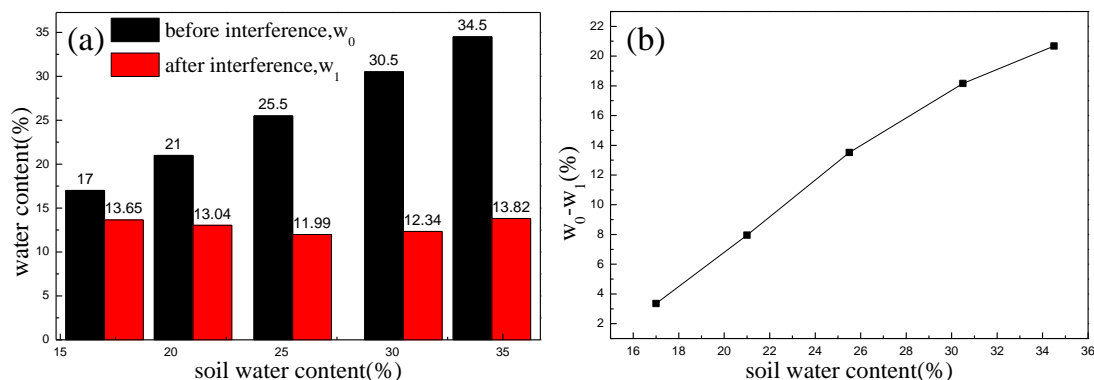


Figure 5. Variation in the soil water content near the surface of the sample before and after 100 V interference (a), and the reduction value of water content after 100 V interference (b)

After the small patch of soil was taken out and weighed, a small amount of deionized water was dripped on the soil surface contacted with the sample, and a pH test paper was dipped in that to obtain the change in the pH value in the local environment of the sample. Figure 6 shows that the local environment turned acidic after the interference. In addition, with increasing original water content, the local environment became more acidic after the interference. At 17% original soil water content, the pH was approximately 6. When the original soil water content was 34.5% , the acidification was the most serious after the interference, and the pH was approximately 2.

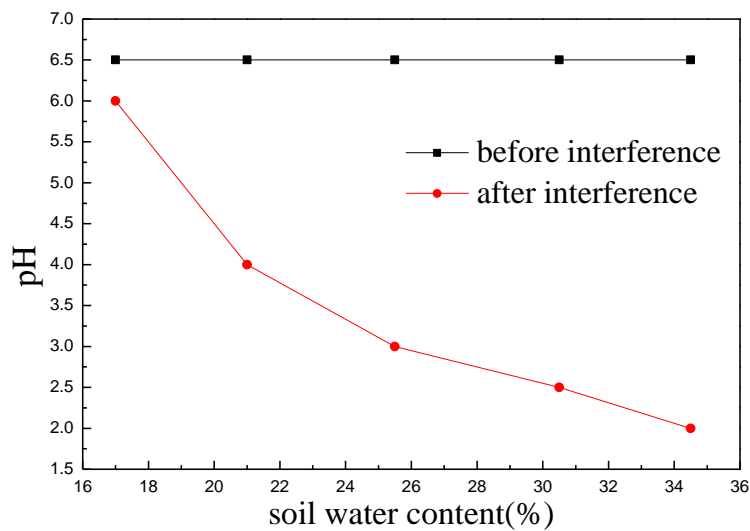


Figure 6. Variation in the pH of the local environment before and after the interference

3.3. Corrosion rate and macroscopic corrosion morphology

After the interference, the corrosion weight loss was measured after cleaning, and the corrosion rate was calculated by formula (2). Figure 7 shows that the corrosion rate increased with increasing soil water content. At 17% soil water content, the corrosion rate was $1.67 \mu\text{m}\cdot\text{h}^{-1}$. When the soil water content was 34.5%, the corrosion rate was $169.49 \mu\text{m}\cdot\text{h}^{-1}$. The corrosion rate of the soil sample with 34.5% water content after the interference was roughly hundred times of that of the soil sample with 17% water content.

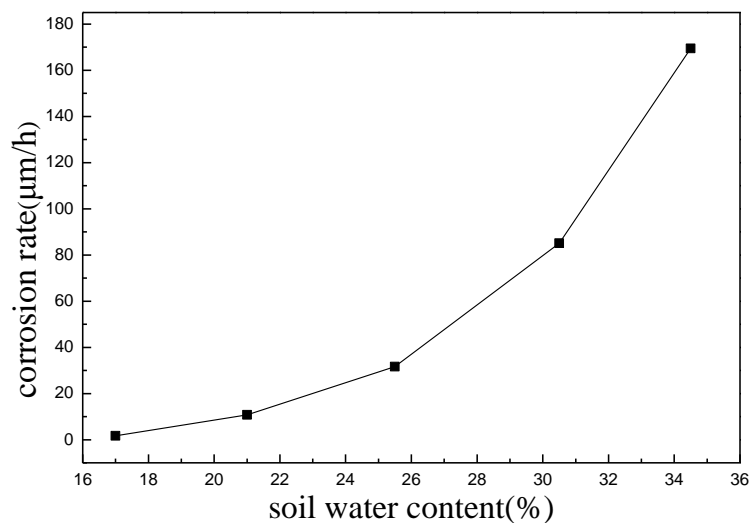


Figure 7. Corrosion rate of X80 steel in clay soil with different water contents after 100 V interference

After the HVDC interference, the macroscopic corrosion morphologies of samples are shown in Figure 8. Figures 8 (A) – (E) show the samples with 17%, 21%, 25.5%, 30.5%, and 34.5% soil

water content. At low soil water content, such as 17% soil water content, only slight corrosion was observed. Red-brown products appeared locally on the surface, and small corrosion pits appeared after cleaning. With increasing water content, such as 21% and 25.5%, corrosion became more serious. A large number of red-brown and black-brown corrosion products interlaced on the surface of the samples, and the rust was loose in texture. After cleaning, uniform corrosion occurred on the surface of the sample and the metallic luster disappeared. With further increase in the water content, such as 30.5% and 34.5%, the corrosion was severe and the corrosion products were mainly black-brown. At the same time, due to the high water content, some soil remained around the corrosion products. After cleaning, the thickness reduced significantly, and the working surface deteriorated obviously.

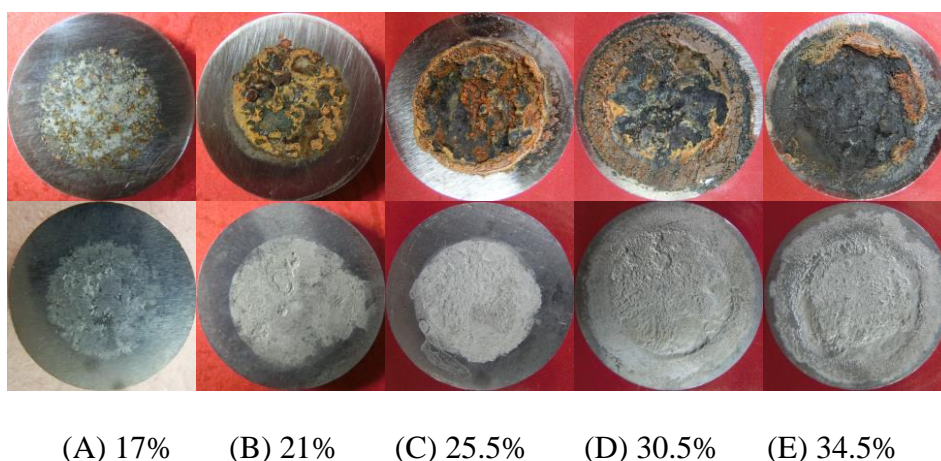


Figure 8. Macroscopic corrosion morphologies of samples after 100 V interference (the upper pictures are after the interference, and the lower pictures are after cleaning)

3.4. Microscopic morphology and composition of corrosion products

After the interference, the microscopic corrosion morphology was observed, and the corrosion products were experimentally determined from the experimental results and compared to the literature data [20–28].

3.4.1. 17% soil water content

The micro-morphologies and compositions of corrosion products after the interference at 17% soil water content are shown in Figure 9. The SEM results showed that some needle or whisker-like structure products appeared on the edge of the irregular rust layer, and some cotton ball structure products were mixed among them. This effectively indicated that these products were the goethite phase (α -FeOOH) [20,22,23]. Besides that, a large number of needle-like products were also found in the inner walls of the larger corrosion pits, and these products were also α -FeOOH [22,23]. At the same time, flat matrix could still be observed in the slightly corroded part, and fine corrosion pits were distributed on it. According to the XRD test results, except the obvious peaks of the iron matrix, the

characteristic peaks of α -FeOOH could be clearly distinguished. Therefore, the analysis showed that when the water content was 17%, the corrosion products were mainly α -FeOOH after the HVDC interference.

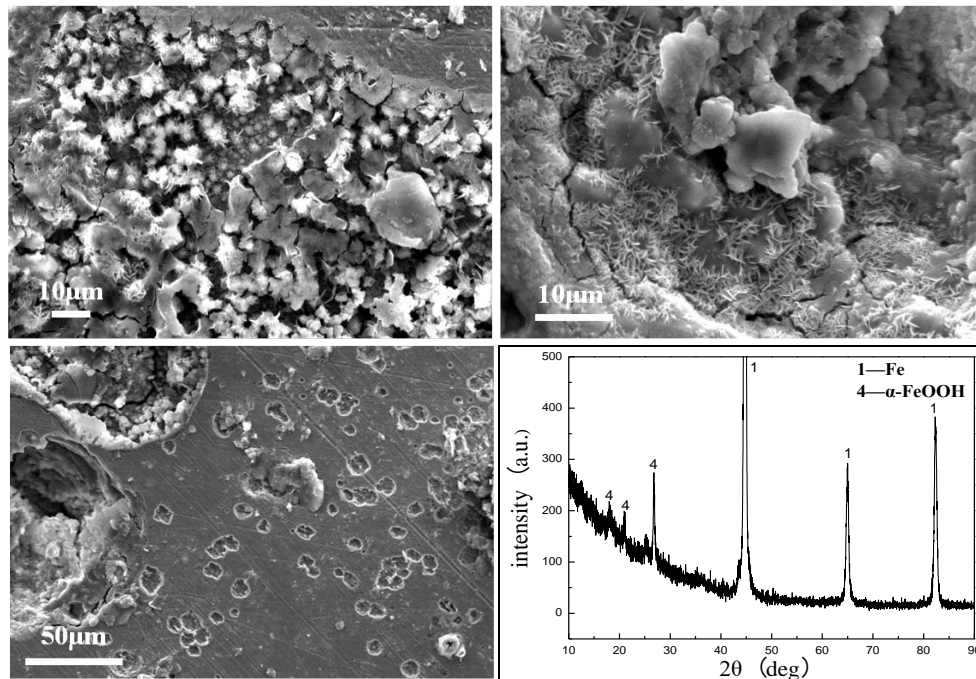
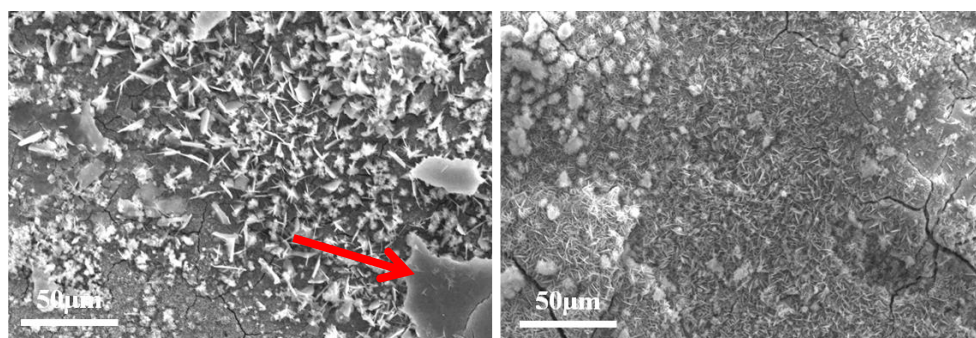


Figure 9. SEM view and XRD of the corrosion products after the interference at 17% soil water content

3.4.2. 21% soil water content

The micro-morphologies and compositions of the corrosion products after the interference at 21% soil water content are shown in Figure 10. The SEM analysis indicates that the products appeared as flowery structures and many fine plates, effectively indicating them as lepidocrocite (γ -FeOOH) [22,23,25,26]. Dark flat regions could be observed in some areas and might correspond to Fe_3O_4 [20,28,29]. Apart from the γ -FeOOH, some cracks appeared in the rust. The XRD results showed that the corrosion products were mainly γ -FeOOH, Fe_2O_3 , and Fe_3O_4 after the HVDC interference.



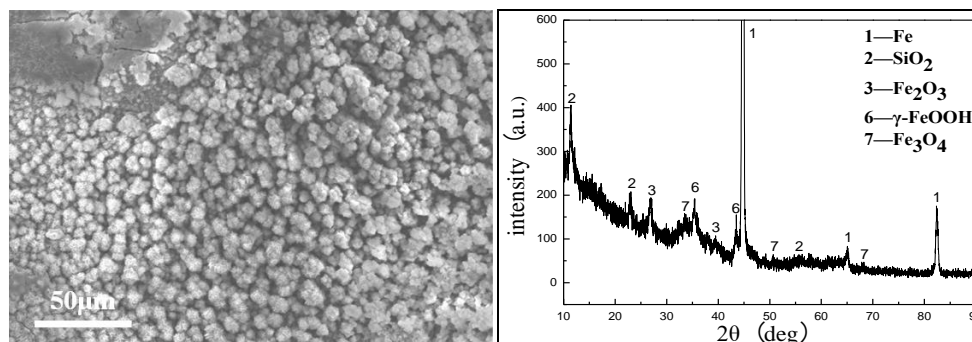


Figure 10. SEM view and XRD of the corrosion products after the interference at 21% soil water content

3.4.3. 25.5% soil water content

The micro-morphologies and compositions of the corrosion products after the interference at 25.5% soil water content are shown in Figure 11. The SEM analysis reveals that products appeared as densely packed plate-like structures, and fragments of a feather-like morphology were observed in some areas. The analysis showed that the products were γ -FeOOH. Apart from the products, more cracks appeared in the rust. At the same time, some areas show a variety of cluttered corrosion products, such as cotton ball-like formations of α -FeOOH, flowery-like formations of γ -FeOOH, and hair-like formations of γ -FeOOH. The XRD results showed that the corrosion products were diverse, with the main components as FeOOH, Fe₂O₃, and Fe₃O₄.

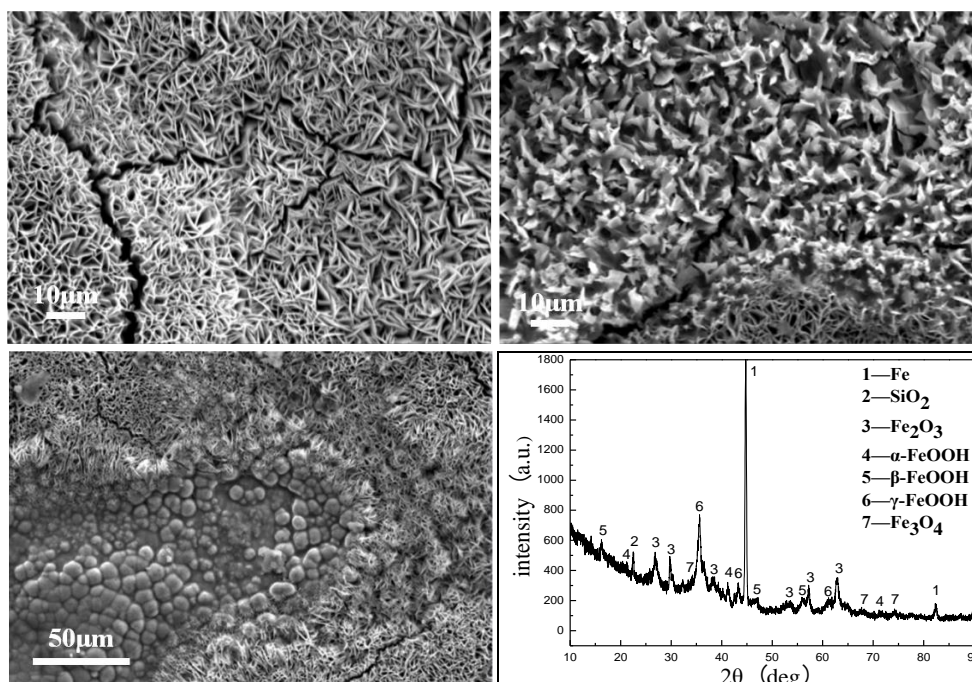


Figure 11. SEM view and XRD of the corrosion products after the interference at 25.5% soil water content

3.4.4. 30.5% soil water content

The micro-morphologies and compositions of the corrosion products after the interference at 30.5% soil water content are shown in Figure 12. The SEM analysis indicates that the corrosion products were spherical and surrounded by fine plates. They were considered as a combination of spherical α -FeOOH and flaky γ -FeOOH. A large number of plate-like structures and more cracks were observed. Observations of a corrosion pit at greater magnification revealed the typical akaganeite (β -FeOOH) crystals structure [21,23,29]. Various corrosion products such as spongy whitish formations of β -FeOOH, cotton ball-like formations of α -FeOOH, and hair-like formations of γ -FeOOH were observed in some areas. The XRD results showed the main corrosion components as FeOOH, Fe₂O₃, and Fe₃O₄.

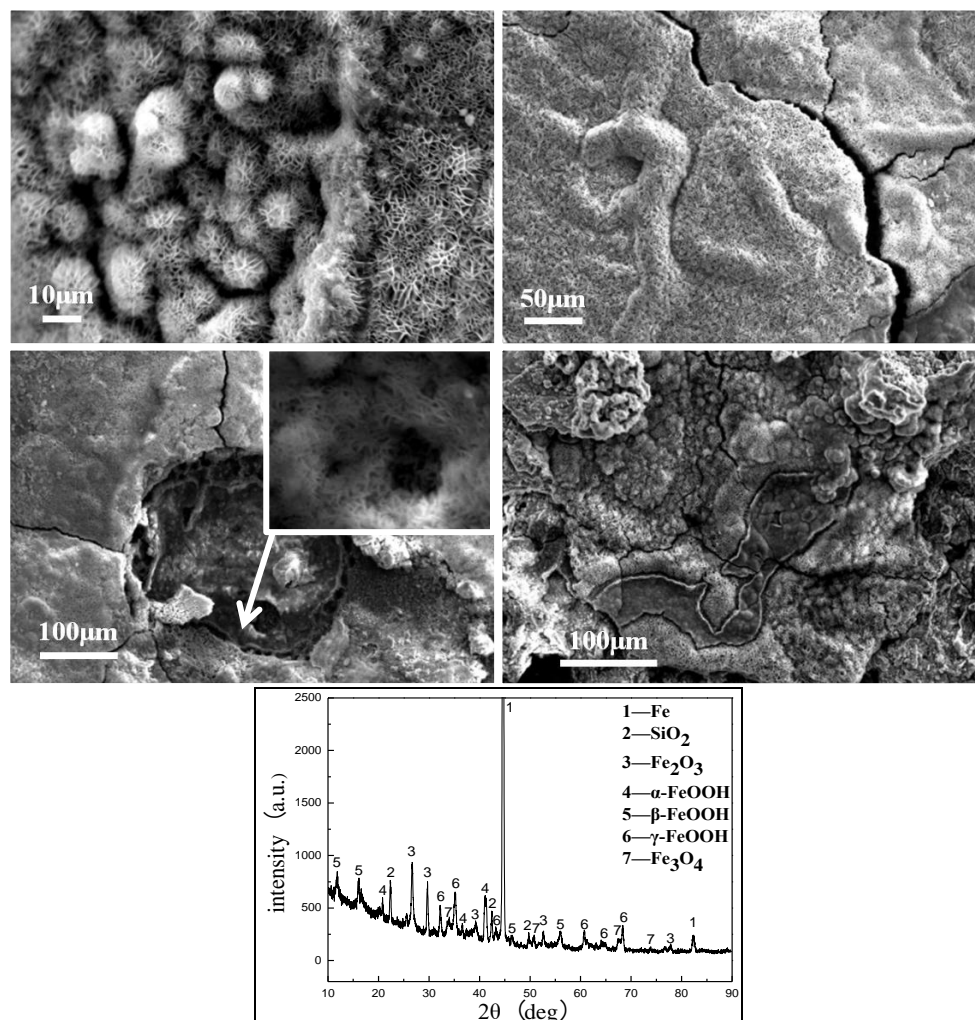


Figure 12. SEM view and XRD of the corrosion products after the interference at 30.5% soil water content

3.4.5. 34.5% soil water content

The micro-morphologies and compositions of corrosion products after the interference at 34.5% soil water content are shown in Figure 13. The SEM analysis indicates that the corrosion products are a large number of irregular products with uniform distribution. The corrosion products were further examined by Energy Dispersive Spectroscopy (EDS), indicating that the Fe:O ratio was approximately 2:3. Therefore, combining with the XRD test results, the corrosion products were mainly found as Fe_2O_3 . Although there were other types of products, their abundance was low.

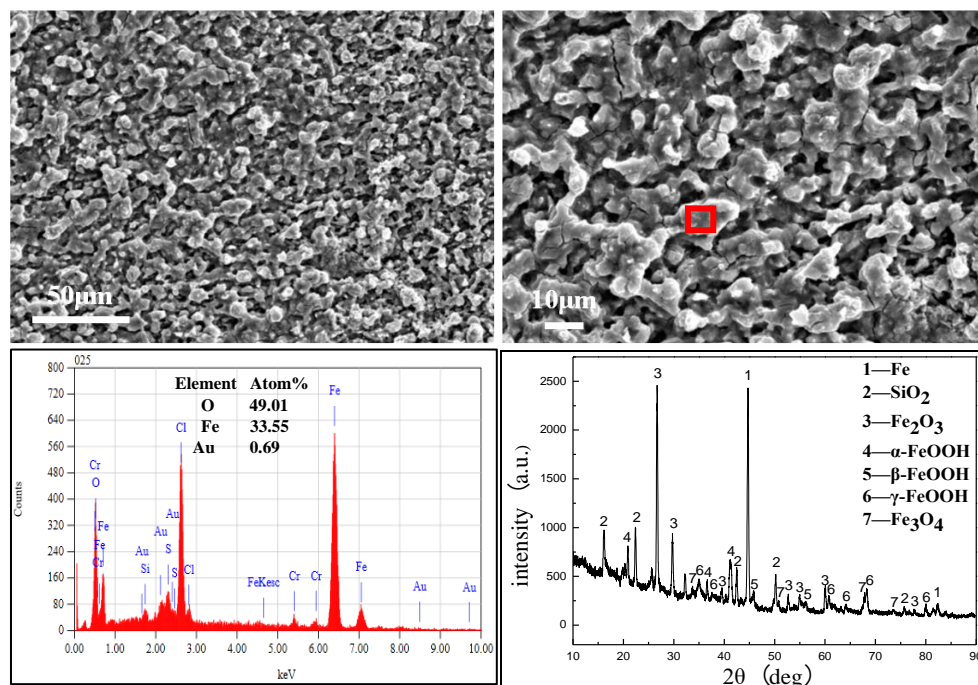


Figure 13. SEM view and XRD of the corrosion products after the interference at 34.5% soil water content

4. DISCUSSION

4.1 Effect of local environmental parameters around sample on corrosion rate in clay soil with different water contents

According to the variation in the local environmental parameters around the samples in Figures 4–7, the properties of local soil around the sample significantly changed by the HVDC interference, and with changing water content, the changes in each parameter were also different. With increasing water content, the temperature of the samples increased during the interference. After the interference, the local soil became acidic, and the resistivity decreased sharply. The test results of the soil parameters showed that the interference made the soil environment around the sample more complex. Nielsen [30,31] believed that the changes in the local soil properties could be reflected by spread

resistance, the change in the resistance between the sample and the reference electrode was related to the shape, size, soil water content, and resistivity of the sample surface. Therefore, the change in the resistance characteristics caused by the local soil environment near the sample under interference could be reflected by spread resistance. Qin [32] also confirmed the correlation between the soil physical properties and DC current density, the change in the DC current density is closely related to the spread resistance. Therefore, a close relationship was observed between the spread resistance and DC current density.

Based on the above analyses, the reasons for DC current density change in different soil water contents are as follows. At low water content, the soil system was stable, and the resistivity was constant before the interference. However, at the instant of electrification, the capacitance of the sample and soil interface completed the charging process quickly, and then the DC current density reached its peak value rapidly, and this period is known as the incubation period of corrosion [33]. At the same time, the conductive soil colloids and ions migrated rapidly in the soil, and the electrochemical reaction occurred at the interface of the sample and the soil, ionization or even electric spark occurred by ion collision under large electric field, increasing the local temperature of the interface, aridity of the soil, and worsened the contact with the sample surface, increasing the resistivity and decreasing the current density. After the current density decreased, the heat release on the sample surface and the water loss decreased. In contrast, the drying of the surface soil would increase the concentration gradient of water, accelerating the water migration to the interface. When the resistivity change caused by the two factors reached a relative balance, the current density could be kept relatively stable. At high water content, the water consumed by the local environment was easily supplemented and the ion migration was easy; therefore, the current density would not decrease.

In addition, the DC current density is an important factor to measure the corrosion rate. According to the DC density curve shown in Figure 3 and Faraday's law, the corrosion rates of X80 with different soil water contents were calculated.

According to Faraday's Law, the theoretical weight loss was calculated by the following formula:

$$w = kIt = \frac{M}{nF} It \quad (3)$$

where w represents the weight loss, k means the electrochemical equivalent of material, I is the DC density, t is the reaction time, M is the mole mass of the material, F is the Faraday constant, and n is the stoichiometric number of electrons consumed in the electrochemical reaction. The following reaction may occur in the soil:



Because the counting frequency of the recorder was 1 s and the working area of the sample was 1 cm², the theoretical corrosion rate could be calculated by integrating the DC density curves. The corrosion rates were compared to the experimental results, as shown in Figure 14. The theoretical corrosion rate calculated by Faraday's law is close to the experimental corrosion rate measured by the weight loss, and the error is small. Therefore, the reaction at the sample surface during the interference is mostly considered as the dissolution of iron metal. The above results show that the corrosion rate can be predicted by measuring the current density, which is of great value in practical engineering.

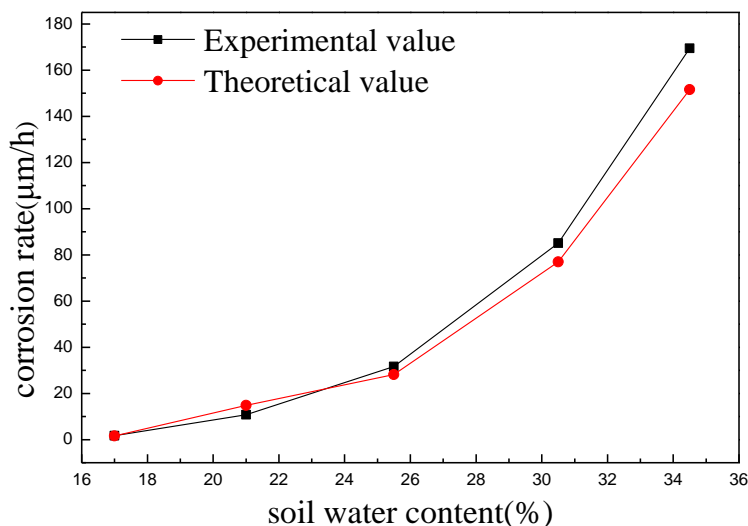


Figure 14. Comparison of the theoretical corrosion rate value with the experimental value

4.2. Corrosion behavior of X80 steel under different soil water contents

The microscopic morphology shown in Figures 9–13 indicates that the main corrosion products were FeOOH and Fe_xO_y at different soil water contents after the interference, but the proportion of each product was different. The schematic of the rust layer formed on the X80 steel surface after the interference is shown in Figure 15. At low soil water content, the corrosion product is mainly α-FeOOH. With increasing water content, the corrosion products are mainly γ-FeOOH and coexistence of various forms of FeOOH and Fe_xO_y, together with some cracks on the rust. With increasing water content, the corrosion product is mainly Fe₂O₃, whereas the abundance of FeOOH decreases.

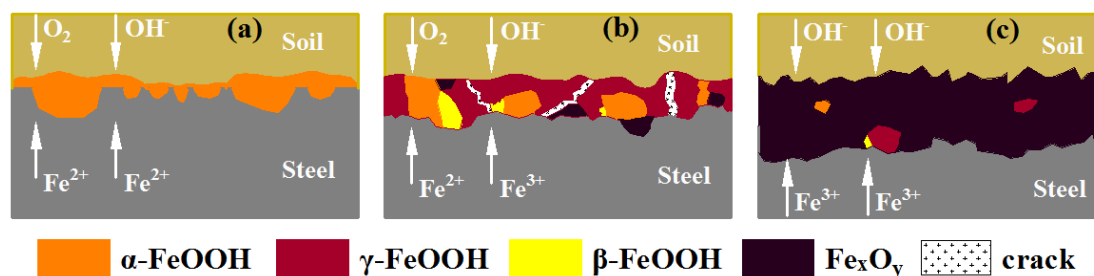


Figure 15. Schematic of the rust layer formed on the X80 steel surface after the interference. (a) Low water content; (b) Middle water content; (c) High water content

The above analyses indicates that the difference in the soil environment affects the corrosion process [13,34,35], and it is reflected by the difference in the DC density, for example, the DC density was about 10 A·m⁻² at stage 3 at 17% soil water content, while the DC density was approximately 200 A·m⁻² at stage 3 at 25% soil water content. Figure 6 shows that at high soil water content, the local

environment turned severely acidic after the interference. Besides, the polarization potential was high during the interference, for example, at 25% soil water content, the polarization potential was 1.12 V_{SCE} at stage 3, and the pH was 3 after the interference, while the polarization potential was less than 0 V_{SCE} , and the pH was 6 after the interference when the water content was 17%. Therefore, the composition of the corrosion products and Pourbaix diagram of the Fe-H₂O system show a relationship between the current density and corrosion products, Fe²⁺ is supplied at a low current density, and Fe³⁺ is supplied at a high current density. Some studies also showed that electrical conditions can affect the formation of corrosion products, for example, Dai [29,36,37] believed that DC electric field would accelerate the growth of γ -FeOOH and inhibit the transformation from γ -FeOOH to α -FeOOH, and the formation of γ -FeOOH and cracks on the surface leads to porous structure, conducive to oxygen transport and accelerate corrosion. Therefore, the growth of γ -FeOOH and the inhibition of α -FeOOH would weaken the protective effect of the rust layer. Qin [28] thought that the DC current density of different strengths had effects on the corrosion products, and high current densities promoted the formation of γ -FeOOH. In addition, among the corrosion products of Fe, the Gibbs free energy of FeO is the highest, belonging the thermodynamically unstable phase. In general, it is preferentially formed, followed by Fe(OH)₂, γ -FeOOH, α -FeOOH, Fe₂O₃ and Fe₃O₄ [38]. The formation of the corrosion products during the HVDC interference in different soil water contents is shown in Figure 16.

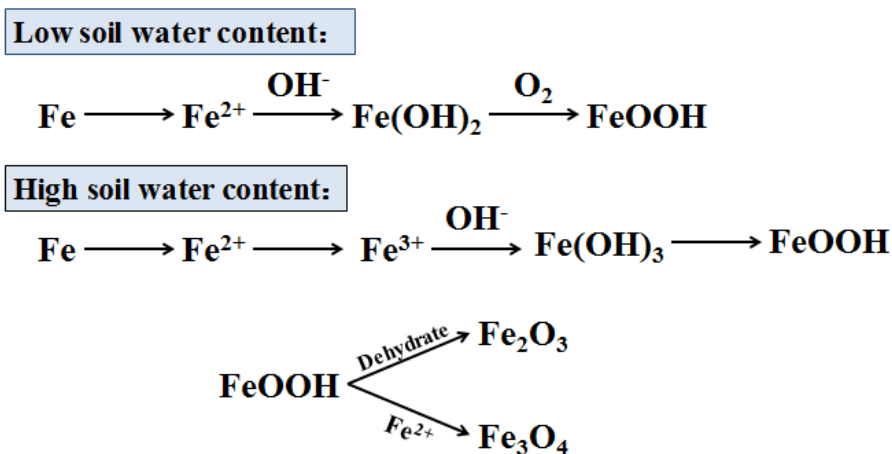


Figure 16. Formation of the corrosion products in different soil water contents

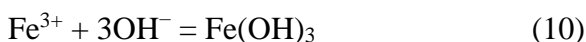
The main reaction processes at low water content are as follows:



The main reaction processes at high water content are as follows:



Because the polarization potential was high, the following reactions might occur.



At high water content, the current density kept at a high level, the heat release was obvious, and the rust layer was dry. Under this environment, the corrosion products were prone to dehydration reaction.



At the same time, some FeOOH reacted with Fe²⁺ dissolved from the anode to form Fe₃O₄.



5. CONCLUSIONS

In this study, the corrosion behavior of X80 steel in clay soil with different water contents under HVDC interference was investigated. The main conclusions are as follows:

(1) Under the HVDC interference, the corrosion rates of X80 steel in clay soils with different water contents are quite different. When the soil water contents were 17%, 21%, 25.5%, 30.5%, and 34.5%, the corrosion rates were 1.69, 10.77, 31.67, 85.13, and 169.49 $\mu\text{m}\cdot\text{h}^{-1}$, respectively. The corrosion rate of X80 at 34.5% soil water content after the interference was roughly one hundred times of that of the soil with 17% water content. Therefore, the water content has an important effect on the corrosion rate.

(2) In low water content environment, the DC current density of X80 steel exhibits obvious three stages variation under large HVDC interference potential. The current density reached sharply to a peak value in a short time when the high DC interference potential was applied, then it dropped rapidly to a lower steady value and maintained for a long time near the stable value. In high water content environment, the DC current density maintained at a high level all the time. Considering the change in the environmental parameters around the sample, the reason for the rapid decrease in the current density at low water content is the increase in the soil temperature, the decrease in the water content, the worse contact with the surface of the sample, and the increase in the resistivity caused by the large DC interference.

(3) According to Faraday's law, the theoretical corrosion rate can be calculated by integrating the DC density curves. The results show that the theoretical corrosion rate calculated by Faraday's law is close to the actual corrosion rate measured by the weight loss, and the error is small. Therefore, calculating the corrosion rate by the DC current density provides a method for predicting the corrosion rate and evaluating corrosion risk under HVDC interference.

(4) The corrosion products were analyzed after the HVDC interference, indicating main corrosion products as FeOOH and Fe_xO_y in soils with different water contents. For soil with low water content, the corrosion product is mainly α -FeOOH. With increasing water content, the corrosion products are mainly γ -FeOOH together with the coexistence of various forms of FeOOH and Fe_xO_y. With further increase in the water content, the corrosion products are mainly Fe₂O₃, while the abundance of FeOOH decreases. The main reason is that different water content leads to different DC current densities, resulting in different temperatures and drying degree of the rust layer, thus resulting in different corrosion products.

ACKNOWLEDGEMENTS

This work was supported by National Key R&D Program of China (Grant No.2016YFC0802101) and China Scholarship Council (Grant No. 201606465052).

References

1. R.Z. Qin, Y.X. Du, Z.T. Jiang and M.X. Lu, *Corros. Sci. Prot. Techn.*, 28 (2016) 263.
2. A.X. Guo, W.J. Hu, A.J. Yan, Z.Q. Yang and L.J. Feng, *Mater. Sci. Forum*, 852 (2016) 218.
3. Z.T. Jiang, G.F. Cao, C.G. Ge, Q.L. Gu, X.Y. Wang and Y.X. Du, Study on the mechanism and influencing factors of HVDC interference, *Nace Corrosion*, USA, 2017.
4. Z.G. Wang, W.J. Wang, F.Q. Wang, X.S. Lan, Z. Geng and Q.Q. Tian, Research on the Corrosion Effect of the UHVDC Ground Electrode Current on the Metal Pipelines, *IEEE International Conference on Power and Renewable Energy*, China, 2016, 48.
5. C.E. Caroli, N. Santos, D. Kovarsky and L.J. Pinto, *IEEE Trans. Power Deliv.*, 5 (1990) 1583.
6. P. Nicholson, High voltage direct current interference with underground/underwater pipelines, *Nace Corrosion*, USA, 2010.
7. R.Z. Qin, Y.X. Du, G.Z. Peng, M.X. Lu and Z.T. Jiang, High Voltage Direct Current Interference on Buried Pipelines: Case Study and Mitigation Design, *Nace Corrosion*, USA, 2017.
8. J.G. Sun, G.F. Cao, C.C. Han, Y.Y. Li, C.G. Ge, L.L. Wang and M.X. Lu, *Corros. Prot.*, 38 (2017) 631.
9. W.X. Bi, H.Y. Chen, Z.J. Li, Y.W. Jiang, L.L. Liu and Y.B. Hu, HVDC interference to buried pipeline: numerical modeling and continuous P/S potential monitoring, *Nace Corrosion*, USA, 2016.
10. R.Z. Qin, Y.X. Du, M.X. Lu, L. Ou and H.M. Sun, *Acta Metall. Sin.*, 54 (2018) 886.
11. C.F. Fu, B.K. Yang, D.N. Yang, J.X. Hu, J. Zhao, E.H. Han and W. Ke, *Corros. Prot.*, 38 (2017) 756.
12. S. Qian and Y.F. Cheng, *Constr. Build. Mater.*, 148 (2017) 675.
13. K.X. Cui, Z.C.J. Ma, Z. Li, Z.X. Bi and X.T. Li, *Pipeline Techn. Eq.*, 5 (2018) 38.
14. T. Huang, X.P. Chen, X.D. Wang, F.Y. Mi, R. Liu and X.Y. Li, *J. Chin. Soc. Corros. Prot.*, 36 (2016) 31.
15. W. Xu, *Chem. Enterp. Manag.*, 31 (2017): 129.
16. L.V. Nielsen and P. Cohn, AC-corrosion and electrical equivalent diagrams, *In Proceedings of the CeoCor*, Belgium, 2000.
17. A.J. Bard and L.R. Faulkner, *Electrochemical methods: fundamentals and applications*, Wiley: New York, (2000) New York, USA.
18. L.V. Nielsen, H. Rosenberg and B. Baumgarten, AC induced corrosion in pipelines: detection, characterization and mitigation, *Nace Corrosion*, USA, 2004.
19. L.V. Nielsen and F. Galsgaard, Sensor technology for on-line monitoring of AC induced corrosion along pipelines, *Nace Corrosion*, USA, 2005.
20. A. Raman, S. Nasrazadani and L. Sharma, *Metallogr.*, 22 (1989) 79.
21. Y.R. Song, G.M. Jiang, Y. Chen, P. Zhao and Y.M. Tian, *Sci. Rep.*, 7 (2017) 6865.
22. D. Fuente, J. Alcántara, B. Chico, I. Díaz, J.A. Jiménez and M. Morcillo, *Corros. Sci.*, 110 (2016) 253.
23. M. Morcillo, B. Chico, J. Alcántara, I. Díaz, R. Wolthuis and D. Fuente, *J. Electrochem. Soc.*, 163 (2016) 426.
24. H. Tanaka, R. Mishima, N. Hatanaka, T. Ishikawa and T. Nakayama, *Corros. Sci.*, 78 (2014) 384.
25. J.G. Castaño, C.A. Botero, A.H. Restrepo, E.A. Agudelo, E. Correa and F. Echeverría, *Corros. Sci.*, 52(2010) 216.
26. Y.T. Ma, Y. Li and F.H. Wang, *Corros. Sci.*, 51 (2009) 997.

27. S.J. Oh, D.C. Cook and H.E. Townsend, *Hyperfine Interact.*, 112 (1998) 59.
28. S. Suzuki, E. Matsubara, T. Komatsu, Y. Okamoto, K. Kanie, A. Muramatsu, H. Konishi, J. Mizuki and Y. Waseda, *Corros. Sci.*, 49 (2007) 1081.
29. N.W. Dai, J.X. Zhang, Q.M. Chen, B. Yi, F.H. Cao and J.Q. Zhang, *Corros. Sci.*, 99 (2015) 295.
30. L.V. Nielsen, Effect of coating defect size, coating defect geometry, and cathodic polarization on spread resistance-consequences in relation to AC corrosion monitoring, *In Proceedings of the CeoCor*, Belgium, 2010.
31. L.V. Nielsen, Role of alkalization in AC induced corrosion of pipelines and consequences hereof in relation to CP requirements, *Nace Corrosion*, USA, 2005.
32. R.Z. Qin, Y.X. Du, Z.T. Jiang, X.Y. Wang, A.Q. Fu and Y. Lu, *Metals*, 8 (2018) 809.
33. M. Tan and Y. Huo, Cathodic protection affected by anodic transients: Critical duration and amplitude, *Nace Corrosion*, USA, 2018.
34. M.C. Yan, C. Sun, J. Xu, J.H. Dong and W. Ke, *Corros. Sci.*, 80 (2014) 309.
35. F.L. Ma, R.Z. Xie, P.J. Han and X.H. Bai, *Int. J. Electrochem. Sci.*, 13 (2018) 5396.
36. N.W. Dai, Q.M. Chen, J.X. Zhang, X. Zhang, Q.Z. Ni, Y.M. Jiang and J. Li, *Mater. Chem. Phys.*, 192 (2017) 190.
37. N.W. Dai, J.X. Zhang, Q.M. Chen, X. Zhang, F.H. Cao and J.Q. Zhang, *Acta Metall. Sin.*, 29 (2016) 373.
38. X.H. Nie, Y.L. Li, J.K. Li and H.B. Zhang, *J. Mater. Eng.*, 8 (2010) 24.

© 2020 The Authors. Published by ESG (www.electrochemsci.org). This article is an open access article distributed under the terms and conditions of the Creative Commons Attribution license (<http://creativecommons.org/licenses/by/4.0/>).